

Accepted for Astronomical Journal;

Adaptive Optics Imaging of Low-redshift Damped Lyman-alpha Quasar Absorbers

Mark R. Chun

Institute for Astronomy, University of Hawaii, Hilo, HI, 96720

Soheila Gharanfoli and Varsha P. Kulkarni

Dept. of Physics and Astronomy, University of South Carolina, Columbia, SC 29208

and

Marianne Takamiya

Dept. of Physics and Astronomy, University of Hawaii, Hilo, HI 96720

ABSTRACT

We have carried out a high angular resolution near-infrared imaging study of the fields of 6 quasars with 7 strong absorption line systems at $z < 0.5$, using the Hokupa'a adaptive optics system and the QUIRC near-infrared camera on the Gemini-North telescope. These absorption systems include 4 classical damped Lyman-alpha absorbers (DLAs), 2 sub-DLAs, and one Lyman-limit system. Images were obtained in the H or K' filters with FWHM between $0''.2 - 0''.5$ with the goal of detecting the absorbing galaxies and identifying their morphologies. Features are seen at projected separations of $0''.5 - 16''.0$ from the quasars and all of the fields show features at less than $2''$ separation. We find candidate absorbers in all of the seven systems. With the assumption that some of these are associated with the absorbers, the absorbers are low luminosity $\leq 0.1L_H^*$ or L_K^* ; we do not find any large bright candidate absorbers in any of our fields. Some fields show compact features that are too faint for quantitative morphology, but could arise in dwarf galaxies.

Subject headings: quasars: absorption lines; galaxies: evolution; galaxies: intergalactic medium; infrared: galaxies; cosmology: observations

1. INTRODUCTION

Damped Lyman-alpha absorption lines in quasar spectra are believed to arise from intervening galaxies and intergalactic matter at various cosmological epochs. The damped Lyman-alpha absorbers (hereafter DLAs) are classically defined as quasar absorbers with $\log N(\text{H I}) > 20.3$ while absorbers with $19.0 < \log N(\text{H I}) < 20.3$ are conventionally classified as sub-DLAs. This distinction is based on the observational constraints of an early spectroscopic study (Wolfe *et al.* 1986). Since the Ly- α line shows damping wings even at $\log N(\text{H I}) \sim 18$ in this paper we will refer to both the sub-DLA and DLAs as DLA systems.

At high redshifts the DLAs are believed to contain a large fraction of the co-moving density of neutral hydrogen in galaxies and possibly account for all of the stars visible today (e.g. Wolfe *et al.* 1995; Peroux *et al.* 2003). The evolution of metallicities in these absorbers provide important probes of the chemical enrichment and star formation history of the Universe (Khare *et al.* 2004; Kulkarni *et al.* 2005). Unfortunately the connection between DLAs and galaxies has not been clearly established. To shed more light on this connection, it is necessary to complement the wealth of spectroscopic data on these absorbers with information on their morphologies, luminosities, colors, and image structure from direct imaging.

It has proven hard to obtain this information for most DLAs. The imaging of high- z DLAs has been very difficult and a large fraction of the attempts to detect the Ly- α emission from high-redshift intervening ($z_{\text{abs}} < z_{\text{em}}$) DLAs have produced either non-detections or weak detections (e.g. Smith *et al.* 1989; Hunstead *et al.* 1990; Lowenthal *et al.* 1995; Djorgovski *et al.* 1996). Imaging studies of low- z DLAs have been more encouraging. Although not always spectroscopically confirmed to be the absorbers, galaxies in images of low-redshift absorber fields often show a variety of morphologies: spirals, irregulars, low surface brightness (LSB) galaxies (e.g., Steidel *et al.* 1994, 1995; LeBrun *et al.* 1997; Bowen *et al.* 2001; Cohen 2001; Turnshek *et al.* 2001). Most of these previous searches had limiting flux sensitivity thresholds of $\sim 0.2L^*$ and thus could not rule out LSBs, while all of the near-IR searches lacked adequate angular resolution to rule out dwarf galaxies close to the line of sight. It is not clear which of the several competing scenarios for DLAs are valid: large, bright, rotating proto-spirals (Wolfe *et al.* 1986; Wolfe & Prochaska 1998; Prochaska & Wolfe 1997b, 1998), gas-rich dwarf galaxies (York *et al.* 1986; Matteucci *et al.* 1997), merging proto-galactic fragments with cold dark matter (e.g., Haehnelt, Steinmetz, & Rauch 1998; Maller *et al.* 2001), collapsing halos with merging clouds (e.g., McDonald & Miralda-Escudé 1999), or low-surface brightness galaxies (Jimenez, Bowen, & Matteucci 1999).

Here we present the first adaptive optics observations of low-redshift DLAs. We have obtained near infrared images of seven absorbers at $0.1 < z < 1.3$ with the University of

Hawaii Hokupa’a adaptive optics system and near-infrared camera QUIRC on the Gemini-North telescope.

We discuss the observations and data reductions in Section 2. The analysis of the data are presented in Section 3 and the results from individual fields are discussed in Section 4. Finally, in Section 5 we characterize our sample of low-redshift DLAs based on our measurements of the sizes, impact parameters, and image structure. Throughout this paper we assume $\Omega_m = 0.3$, $\Omega_\Lambda = 0.7$, and $h = 0.73$.

2. OBSERVATIONS AND DATA REDUCTION

2.1. OBSERVATIONS

Our sample consists of seven low-redshift absorption systems that have confirmed Lyman-alpha absorption features. The redshift range was constrained so that hour long exposures would reach limiting magnitudes representative of low surface brightness features at the redshift of the absorption systems. The most stringent observational constraint was set by the AO system’s requirement that the target field have a sufficiently bright wavefront reference source for the adaptive optics system ($R \leq 17$) to provide a useful correction. In total six fields with seven absorption systems were observed. We present the object field properties in Table 1 where we have preserved the nomenclature of DLA and sub-DLA for reference.

Between August 2000 and April 2001, we observed the fields around the six quasars in the H or K’ filter (Wainscoat & Cowie 1992) with the now-decommissioned University of Hawaii 36-element curvature adaptive optics (AO) system (Hokupa’a) (Graves et al. 2000) on the Gemini-North telescope. In all cases the quasar was used as the wavefront reference source for the AO system. The University of Hawaii near-infrared camera QUIRC (Hodapp et al. 1996), containing a 1024×1024 pixel HgCdTe detector, with a pixel scale of $0''.020/\text{pixel}$, was used as the focal-plane imager. All data were taken in better than one-arcsecond seeing conditions with two fields observed under photometric conditions. Table 2 summarizes the observations.

Each field was observed as a dithered series of short exposures, each exposure being 30-180 seconds long. The sides of the dither pattern were $5''$ resulting in a final mosaic image with an area approximately $15'' \times 15''$ in the deepest exposure region. The dither size of $5''$ was a compromise between having as large a deep-exposure field as possible and having a separation large enough to generate a sky frame from the on-source data. After each cycle through a five-point dither pattern, we offset the telescope by roughly $0''.1$ and repeated the dither pattern. This offset was used to ensure that groups of bad pixels could

be removed in the data reduction. This combination of offsets and dithers was carried out until we obtained the total exposure times.

The final mosaic images have quasars with FWHM from $0''.2$ to just under $0''.5$. This should be considered as a rough estimate of the image resolution since in general the quasar is not a point source but may contain a bright host galaxy.

2.2. IMAGE DATA REDUCTION

Standard data reduction techniques for near infrared imaging were used to produce the final images. Individual frames were sky-subtracted and flat-fielded. Separate sky frames were constructed for each individual exposure by averaging source-masked dithered frames taken within 10-20 minutes of the individual exposure. Flat-fields were constructed from dome flat images with the lamps on and off. We favor the use of the dome flats over sky flats because sky flats constructed from the object images do not account for the emission from dust on the telescope and instrument surfaces. This is especially important in the K' where the difference between the sky flats and the dome flats were as much as several percent. Bad pixels were identified as hot pixels in short dark frames, as dead pixels in flat frames, and as pixels with large standard deviations in either of the dark or flat sequences.

Individual frames were registered to the nearest pixel using the centroid of the quasar and averaged excluding bad pixels and $\geq 3\sigma$ deviations in the stack. The integer pixel registration is more than sufficient for this data since in all cases we have 7-20 pixels across the FWHM of the images. No correction was made for field distortions in the Gemini/Hokupaa/QUIRC images as these are small (Rigaut 2005).

2.3. SUBTRACTION OF THE QUASAR POINT SPREAD FUNCTION

In order to properly study the area near the quasar, we need to remove the contribution to the image of the quasar and its host galaxy. This problem depends critically on our knowledge of both a point spread function (PSF) not well described by an analytic function and on the intrinsic nature of the quasar and its host galaxy. This section describes the QSO-subtraction techniques we used.

First, during the observation we observed stars as PSF calibrations. These PSF calibration targets were chosen to have a similar right ascension, declination, and visual magnitude as the wavefront reference sources (e.g. the quasars). Observations of the PSF calibration fields were made interspersed with those of the quasar fields to sample the changes in the in-

trinsic atmospheric seeing. In all cases, the shape of the calibration PSF did not match point sources in the quasar field. This occurred for several reasons. First, at the faint magnitudes of these guide stars the correction of the adaptive optics system depends strongly on the photon flux in the wavefront sensor. While we attempted to select nearby stars with similar catalog magnitudes, matching the wavefront sensor counts was in practice quite difficult and the wavefront sensor photon flux was typically matched to no better than 10 – 20%. Second, while we observed the PSF calibration fields interleaved with the quasar field, the timescale for seeing changes can be as short as a few minutes. This is too short for the PSF calibration star observations to, in practice, be made under exactly the same atmospheric conditions. Third, the calibration stars were faint in the H/K' bands and required long exposure times to reach a SNR at large radii to make them useful for PSF subtraction. This was unrealistic given the overheads required.

To circumvent these problems, we attempted three techniques to generate PSFs directly from the data. First, for quasar fields containing a stellar source we have a PSF which was taken under identical atmospheric conditions. However, for all of the observed fields, the quasar is the brightest source so the signal-to-noise ratio at large radii in these stellar images did not match that of the quasar. In addition, in the few fields with stellar sources, the sources happen to be only a few arcseconds from the quasar. While this is well within the corrected field of view of the adaptive optics system (Chun 1998), extracting a clean PSF to a radius containing most of the stellar flux proved difficult. Knowledge of the PSF at these large radii is important because the PSFs can have a significant fraction of energy outside their core. For example, the average 50% encircled energy diameter was 0''.59 in the H band and 0''.28 in the K' band.

Given that the quasar is the brightest object in the observed fields, we tried constructing a PSF from an azimuthally averaged image of the quasar itself. The azimuthally averaged profile is computed directly from the final image and, by construction, is not subject to differences in the guide star brightness or to variations in the intrinsic seeing. The resulting PSF-subtracted image is similar to an unsharp mask but here the smoothing is done azimuthally. The technique assumes that the light near the quasar is well represented by the azimuthal average. Asymmetries in the PSF can arise from astrophysical sources (e.g. a host galaxy) as well as instrumental sources (e.g. telescope windshake). In many cases the residual in the azimuthally-averaged PSF subtracted image contained one pair of symmetric positive flux lobes and another pair of symmetric negative flux lobes.

Finally, we constructed models of the PSFs using a principle component analysis or Karhunen-Loeve (KL) decomposition. The Karhunen-Loeve decomposition has been previously used to quantify PSFs by Lupton *et al.* (2001) and Lauer (2002). Lauer (2002)

suggested using the KL decomposition to quantify the field variations of the PSF of adaptive optics systems. Here, we have applied this technique to quantify the modes in which the PSF varies with time. The basic idea is to construct a basis function that characterizes the temporal variations of the image of the quasar. Any component in the final quasar image well fit by this basis function is assumed to be due to the AO PSF changing and is removed from the final quasar image. The Karhunen-Loeve decomposition provides the means to construct the basis function. A $4'' \times 4''$ region centered on the quasar in each of the individual reduced frames was binned 2 pixels, normalized, and centered on the quasar. From this set of images (P_i), we construct the basis function by calculating the eigenvectors and eigenvalues for the PSF covariance matrix:

$$Covar_{i,j} = \langle P_i P_j \rangle \quad (1)$$

Each eigenvector represents a mode in the basis function and the eigenvalue represents the relative importance of each mode in the basis set. Once the basis function is determined, the quasar in the final image can be reconstructed using the first few modes (typically ~ 30) with the largest eigenvalues of the basis function. These first few modes are by virtue of the Karhunen-Loeve expansion the modes with the most variance within the data set. In using this reconstructed model PSF, we can in principle erroneously interpret some underlying parts of the true light from the quasar, host galaxy, or absorber galaxy as a component of the PSF since some modes of the basis function could be similar to these light distributions. Since we have constructed the basis set from the covariance matrix, the modes of the basis set describe image structure that changes with time. Faint diffuse objects are less sensitive to changes in the image PSF than small unresolved objects.

For each quasar field we generated a KL basis set and then fit the image of the quasar in the final mosaic image with the first 30 modes. This model quasar was then subtracted from the field to look for objects close to the line of sight of the quasar. In fields with known stellar components we also fit the final stellar image with this same basis set as a measure of the residuals in the PSF subtracted images.

Figure 1 shows a comparison of the techniques we used to remove the contribution of light from the quasar. Each of the four columns in the figure show a different technique applied to the quasar and to the point-source just South of the quasar in the Q0850+440 field. The cleanest quasar subtraction is using the KL PSF though this analysis is CPU intensive and could only be applied within a couple of arcseconds from the quasar. Residuals in the stellar image subtraction extend to a radius of about $0''.5$. We take this radius as the minimum separation from the quasar line of sight for an object to be detected with this technique. As simple and as fast as it is, the azimuthal averaged quasar image worked

surprisingly well. While the intensities in these residual images were larger than those in the KL QSO-subtracted image by a factor of two, the extent of the residuals were nearly identical.

Figures 2-7 show the reduced image and the QSO subtracted image for each field. For fields where HST archival imaging data are available, we show the HST images for comparison. These archival data are from the HST programs of Bahcall (proposal ID: 5343, Q0054+144), Burbidge (5096, Q0235+164), Lanzetta (5949, Q0850+440), Bechtold (9173, Q1127-145), and Steidel (5984, Q1329+412).

3. ANALYSIS

3.1. OBJECT DETECTION

We used the automated software SExtractor (Bertin and Arnouts 1996) to detect sources in our images. We ran SExtractor on the regions with the highest signal-to-noise ratios of the azimuthally-averaged QSO-subtracted images. These regions spanned approximately $15''$ on each side. In addition, we ran SExtractor on the regions centered at the position of the quasar in the KL quasar-subtracted images. These smaller regions measured $4'' \times 4''$. To look for extremely faint objects, we ran SExtractor on the smoothed images. In this latter case, we used the azimuthally-averaged quasar subtracted images and convolved the images with a gaussian with a FWHM of 20 pixels ($0''.4$).

SExtractor requires a number of input parameters to work properly. Naturally, the driving parameters are the detection threshold and the number of connected pixels above that threshold. After many test runs, we chose a detection threshold per pixel of 1σ of the sky level and a minimum number of contiguous pixels of 75. Connected pixels are defined as pixels touching any of their sides or corners as implemented in SExtractor. Thus for a detection to be triggered, there had to be 75 connected pixels each with an intensity at least 1σ above the sky. Our 1σ per pixel threshold corresponds to a surface brightness of $\mu_{1\sigma,lim} \sim 20.0 \text{ mag/arcsec}^2$ in H and $\mu_{1\sigma,lim} \sim 19 \text{ mag/arcsec}^2$ in K' (Table 2). In comparison, the sky brightness in H at Mauna Kea is $\mu_H \sim 13.4 \text{ mag/arcsec}^2$ (Tokunaga 1999) and $\mu_{K'} \sim 12.8 \text{ mag/arcsec}^2$ (Gemini Hokupa'a instrument web page) thus our limiting surface brightness is $\sim 300 - 400$ times fainter than the sky.

At these flux limits, we expect to be able to measure image structure for the brighter disk galaxies and to detect dwarf galaxies. Disk galaxies in the Coma cluster have typically

$\mu_e^1 = 17.2$ mag/arcsec² Gavazzi *et al* (2000) so that at the target absorbers with $z \leq 0.2$, we expect disk galaxies to have μ_e in the range 20.2 - 21.7 mag/arcsec². These are just at the surface-brightness limit of our data. Our object detection threshold is much fainter. For example, Virgo cluster dwarf galaxies have a median total H ~ 12 mag (Gavazzi *et al.* 2001) and would measure $H \sim 20$ mag at the redshifts of our sample, assuming a flat spectrum. The limiting magnitude of our observations, defined as the magnitude corresponding to a 3σ flux within an aperture of 75 pixels, is approximately $H_{3\sigma,lim} \sim 23.3$ and $K'_{3\sigma,lim} \sim 21$ (see Table 2). At our flux limits we easily detect typical dwarf galaxies at the redshifts of these absorbers.

The detected sources are presented in Table 3. We detect a total of 31 sources around 6 quasars. The naming convention for objects corresponds to the offset east and north in arcseconds from the quasar centroid. Each of the six quasar fields contains at least one object and five of the six fields show objects previously undetected.

3.2. Photometry

Absolute photometry is based on observations of standard stars taken during the same night before and after the observations of the quasar field when observing conditions were photometric. For data obtained under non-photometric conditions, we used the quasar and its 2MASS catalog magnitude to boot-strap the photometry of the objects in the fields. This is reasonable as long as the quasar is not highly variable in the near-infrared. There are two cases when the night was not photometric and the quasar is known to be highly variable. For Q0235+164 we report relative photometry only. In the case of Q1127-145, we used the photometry of object G1 from Chen *et al.* (2001) kindly provided to us by Hsiao-Wen Chen to boot-strap the photometry for the rest of the objects in the field.

All photometry is reported here as AB magnitudes. The following relationship between the Vega and AB systems (Oke & Gunn 1983) was used:

$$m_{AB} = m_{Vega} - 2.5 \log(f_{\nu,0}) + 8.90 \quad (2)$$

where the zero-point flux is taken to be $f_{\nu,0} = 1080$ Jy in H and $f_{\nu,0} = 670$ Jy in K' (Tokunaga 1999). In Table 3, we list for each detected object the ID (right ascension and declination offsets relative to the quasar); the angular distance to the QSO, $\Delta\theta$ in arcsec, and the AB magnitude in the H or K' band as determined by SExtractor. These are the

¹ μ_e is the surface brightness at the half-light radius

magnitudes determined using a metric radius defined as 2.5 times the first moment of the light profile (Kron 1980): $r_{metric} = 2.5 \times \int I(r)rdr / \int I(r)dr$ where $I(r)$ is the intensity profile as a function of radius r .

3.3. Image Structure

The image properties of the detected sources allow us to characterize their morphologies and to address the question of whether they are bulge-dominated or disk-dominated. We determined the structural parameters for roughly half of the detected sources by running GIM2D (Simard *et al.* 2002) on the azimuthal-average subtracted images. Out of the 31 sources detected, we were able to extract image structural parameters for nineteen sources. Fourteen sources had high total signal-to-noise ratio and are well separated from the quasar. For five of the sources, the structural parameters are largely uncertain (as seen by the errors in Table 4). The remaining objects were either too faint or too close to the quasar line of sight to estimate any image structural parameters. In the end, we are able to constrain the morphologies of twelve out of the 31 sources.

GIM2D fits two dimensional intensity profiles with a combination of the Sérsic law and an exponential disk. Each source was fit with three types of models: (1) single $r^{1/n}$ -laws, (2) exponential disks plus $r^{1/4}$ -laws, and (3) exponential disks plus $r^{1/n}$ laws. In all cases the PSF provided to GIM2D was the azimuthally-averaged quasar image.

The output quantities of GIM2D include the total luminosity, bulge-to-total ratio (B/T), effective radius (r_e), ellipticity of the bulge, position angle of the bulge, exponential disk scale length (r_d), inclination angle of the disk, position angle of the disk, x and y position offsets, background level, reduced- χ^2 value, half-light radius, and Sérsic exponent n . These values are provided with their 99% confidence limit. If the distributions were normal, they would correspond to a 3σ error. We assign a morphological class based on the values of B/T , r_e , r_d , and n and their 99% confidence limits. Table 4 presents the derived image structural parameters for each object. We list the objects' ID, the bulge/disk ratio (B/T), the scale lengths (r_e and r_d) in arcseconds, and the exponent n of the generalized $r^{1/n}$ -law. For the bulge-to-total ratio, scale lengths, and exponent, we also present the 99% confidence limits obtained with GIM2D.

An important motivation for the study was to determine whether bulges or disks dominated galaxies account for the low-redshift absorbers. As such, in assigning a morphological type, we identified the objects as point sources, disk-dominated, bulge-dominated, or a combination of disk and bulge. Of the sources we could measure the structural parameters, 3 of

them have FWHM that are identical to the PSF. For these sources, GIM2D returned zero scale lengths and we interpret these as point sources. Single $r^{1/n}$ fits were used to determine if any of the sources were pure disks. A pure disk would have a value of $n = 1$ in the Sérsic-law only fits. We found that only two sources are consistent with being pure disks. We found $n = 0.96_{-0.05}^{+0.75}$ for Q0235+164 -5.85-2.69 and $n = 1.43_{-0.20}^{+0.12}$ for Q1127-145 +14.5-6.76. These values are also consistent with the fits done with two components (see Table 4) where they have a small bulge ($B/T < 0.27$) and large disk scale length ($r_d \sim 0''.2$).

The outputs of the $r^{1/4}$ and the generalized $r^{1/n}$ fits are consistent with each other within the confidence limits. By and large we found that the $r^{1/n}$ +disk fits showed a smaller residual signal and we therefore provide the results of these decomposition instead of that of the $r^{1/4}$ +disk. Even though we allowed n to vary, 10 of the sources returned $n \sim 4$ as the best fit. We used the reduced- χ^2 values that are output by GIM2D to discard any bad fits. There are only two cases in which the reduced- χ^2 values are large. From the two component fits, we find that there are 6 disk-dominated galaxies, 3 disk+bulge galaxies, 2 bulge-dominated galaxies, 3 point sources, and 5 unconstrained objects.

4. RESULTS

Below we present the astrometric, photometric, and morphological results derived for the features in each field. Table 5 summarizes the morphologies, impact parameters, luminosities, and scale lengths for the candidate objects, assuming that they are at the redshifts of the absorbers. The morphology is not listed for the objects that are too faint or too close to another object, since the profile fits for these objects are not robust. The scale lengths of the profiles are not listed for the point sources and for the sources where the profiles could not be fit. For candidate absorbers, we converted fluxes to luminosities using $L = 4\pi d_L^2 F$ where d_L is the luminosity distance of the DLA candidate. These luminosities are expressed in units of L^* where we have adopted $L_H^* = 1.33 \times 10^{43} \text{ erg s}^{-1}$ (Kulkarni *et al.* (2000)) and $L_K^* = 3.62 \times 10^{42} \text{ erg s}^{-1}$ (Bell *et al.* (2003)).

4.1. Q0054+144

Q0054+144 is a radio-quiet X-ray-bright QSO at a redshift of $z_{em} = 0.171$. This object was imaged with HST WFPC2 (Bahcall *et al.* 1996; McLure *et al.* 1999). These HST data indicate that the host galaxy is well described by an early-type galaxy. A DLA candidate absorber at $z = 0.103$ with a neutral hydrogen column density of $\log N(\text{H I}) = 20.1$ was

suggested by Lanzetta et al. (1995) using IUE data. However, higher resolution HST GHRS spectra showed that no DLA absorption is present at $z = 0.103$ (Bechtold et al. 2001) and no X-ray absorption was detected in Chandra observations of Bechtold et al. (2001). A low-ionization metal absorption line system is present at $z = 0.103$, but the Ly- α line is not damped, with $\log N(\text{H I}) = 18.3$ (Turnshek & Rao 2002). Thus this is a Lyman-limit system.

Figure 2 shows our H-band image of the field, the quasar-subtracted image of the central portion of the field, and the HST/WFPC2 F606W image. Our H-band image is $20'' \times 20''$ which corresponds to $\approx 40 \times 40 \text{ kpc}^2$ at $z = 0.103$. We detect an object approximately $0.8''$ SW of the quasar only after the KL QSO subtraction. It is too close and too faint to measure its magnitude or structural parameters. It is in the same direction and approximately the same location as the object identified in (?) (See their figure A11) but is considerably less extended. This smaller extent may be due to the smaller region over which the quasar subtraction was applied with the KL technique. In addition, a number of faint objects are seen around this elliptical galaxy in both our image and the HST image. They are all small objects and could be companions to the host galaxy. An additional object lies approximately $12''$ south of the quasar just at the edge of our field of view and appears to correspond to an object in the HST image of McLure et al. (1999). This object was excluded from our analysis due to its close proximity to the edge of our field.

4.2. Q0235+164

Q0235+164 (AO 0235+164) is a radio-loud, optically violently variable, X-ray and γ -ray emitting blazar. Roberts et al. (1976) measured a complex 21-cm absorption profile in the radio spectrum of AO centered at $z = 0.524$. Based on a UV spectrum of the QSO obtained with HST/STIS, Cohen et al. (1999) confirmed that the absorber is a DLA with $N_{\text{HI}} \approx 5 \times 10^{21} \text{ cm}^{-2}$. Junkkarinen et al. (2004) have detected the 2175 \AA feature and diffuse interstellar bands at the redshift of this absorber. Two faint objects with [OII] 3727 emission, have been detected within $2''$ from AO, and have been suggested as possible sites for the $z = 0.524$ absorption system (Smith et al, 1977; Yanny et al, 1989). Burbidge et al. (1996) using HST/WFPC2 and HST/FOS resolved these two objects more clearly. The nearest one (Yanny *et al.* (1989)'s A1) might contribute to the complex H I 21-cm absorption, while the object $2''$ south of AO (Yanny *et al.* (1989)'s A) is an AGN surrounded by faint nebulosity which can be classified as a BALQSO. In the optical and infrared imaging observations of the QSO, Chen & Lanzetta (2003) concluded that there is a group of galaxies at the redshift of the known DLA several of which likely contribute to the DLA system. They find that the photometric redshift for the object $2''$ south of the QSO is consistent with the spectroscopic

redshift of the known DLA. Yanny *et al.* (1989) found [O II] emission from both the A1 and A objects.

Figure 3 shows our H-band image of the field before and after subtraction of the quasar image as well as the archival HST/WFPC2 F702W image. The full images are $20'' \times 20''$ corresponding to $\approx 120 \times 120$ kpc² at $z = 0.524$. We identify six objects. The angular distances of these objects to the QSO range from $\Delta\theta = 0.6''$ to $10.2''$ corresponding to $b_{abs} = 3$ to 60 kpc. Objects other than object -4.93-7.47 have already been reported in the literature. It is unlikely to be the absorber since at the redshift of the absorber it would have an impact parameter of more than 50 kpc and its profile scale length is close to the FWHM of the quasar. Object -7.15-7.21 appears to be a point-source in the HST images but shows a linear extension in both our H-band image and the HST image. Object +0.15-1.91 is the BALQSO object found by Burbidge *et al.* (1996). Its morphology in the NIR is extended and disk dominated. An object is detected by SExtractor in the PSF subtracted image at a separation of $0.5''$ from the quasar centroid (-0.3-0.4). We have disregarded this object since it falls within the region where PSF residuals are seen in PSF subtractions of stellar images.

We regard +1.11-0.01 (object A1 in Burbidge *et al.* (1996)) as the likely absorber. Its photometric redshift is consistent with it being at the absorber redshift (Chen and Lanzetta 2003) and its profile is consistent with a combination exponential disk and $r^{1/4}$. Absolute photometry was not possible from our data for this field because of the observations were made under nonphotometric conditions. SExtractor identifies another object $2.5''$ NE of the quasar. This object was not reported in previous studies. While SExtractor identifies this and object +1.11-0.01 as separate objects, a 1-D cut across these two objects is well fit by a bulge+disk profile. If these are the same object, then it could be a spiral galaxy slightly inclined to our line of sight. At the redshift of the absorber, it would have an impact parameter of about 6-7 kpc. We note that if the object +2.40+0.93 is an extension of object +1.11-0.01, then the extension is in the NE direction. This is perpendicular to the orientation suggested by Burbidge *et al.* (1996).

4.3. Q0738+313

Q0738+313 (OI 363) is a core-dominated slightly variable quasar at $z_{em} = 0.635$. Rao *et al.* (1998) reported the discovery of two DLA systems toward the quasar at $z = 0.0912$ and $z = 0.2212$ with $N(H I) = (1.5 \pm 0.2) \times 10^{21}$ and $(7.9 \pm 1.4) \times 10^{20}$ cm⁻², respectively. They concluded that a galaxy at $5.7''$ from the QSO line of sight is the only reasonable candidate at either absorption redshift. Cohen (2001) reported galaxies at $z = 0.221$ and

$z = 0.106$, $6''$ and $28''$ away from the quasar line of sight, respectively. She suggested that the $z = 0.106$ galaxy may be a member of a cluster that causes the absorption at $z = 0.0912$. The morphology of this galaxy was classified as early-type by Rao *et al.* (1998). Optical and infrared imaging observations of the QSO made by Turnshek *et al.* (2001) indicate that the DLA galaxy at $z = 0.2212$ is a “faint neutral colored galaxy with dwarf galaxy-like K and B-band luminosities.” Its spectrum is that of an early-type galaxy. Turnshek *et al.* (2001) also suggested that the putative $z = 0.0912$ DLA galaxy is likely to be all or part of the resolved light surrounding the quasar with armlike and jetlike-features. They suggested that the DLA is a low surface brightness dwarf galaxy, possibly an irregular or interacting system.

Six objects are detected in our image. Five have previously been identified. Object +1.90-5.38, the dwarf galaxy at $z = 0.221$ and designated “G1” by others (Cohen 2001; Turnshek *et al.* 2001) is a disk-dominated galaxy with a bulge-to-total ratio of 0.34. This is consistent with an E/S0 galaxy suggested by Turnshek *et al.* (2001). The object +2.02+1.54, designated “S1” by Turnshek *et al.* (2001), is still unresolved in our images, and GIM2D identifies the object as a point-source.

The faint arm and jet-like features discussed by Turnshek *et al.* (2001) are not apparent in our unbinned image. While our image has an angular resolution of about $0.2''$, our 1σ per pixel limiting surface brightness is $18.9 \text{ mag/arcsec}^2$. The arm and jet like features discussed by Turnshek *et al.* (2001) are about two magnitudes fainter. In order to achieve this sensitivity, we smoothed the image with a gaussian with a FWHM equal to the FWHM of the quasar image, subtracted an azimuthally-averaged PSF, and rebinned the image to $0.2''$ pixels. The resulting image is shown in the lower-right panel of Figure 4. In this image we used an azimuthally averaged PSF to subtract the light from the quasar because the KL analysis could not be performed over this large a field due to its computational requirements. The quasar contribution at the separation of the jet and arm are small so this subtraction should be adequate. This image was then analyzed by SExtractor. The feature +5.40-0.11 east of the quasar is aligned with the bright knot in the Turnshek *et al.* (2001) “arm” but the linear feature WSW of the quasar is found to be slightly rotated from the position shown in Figure 1 of Turnshek *et al.* (2001). In our image the linear feature extends along a line intersecting the quasar whereas in Turnshek *et al.* (2001) the feature appears aligned east-west. The jet clearly shows a highly mottled linear morphology.

A new feature, +0.71+01.63, can be seen in the smoothed and binned image (Figure 4). It is also seen in the KL PSF subtracted image when it is similarly smoothed and rebinned. This feature is previously unidentified. It appears to have a core with faint emission extending several arcseconds to the NNW. It is not clear whether this emission is some component of

a larger object encompassing all the faint nebulosity but given its close proximity to the quasar line of sight ($b=3$ or 6 kpc), it is likely to be associated with one of the absorption line systems.

The feature seen less than $0.5''$ SW of the quasar line of sight in the KL PSF-subtracted image is a possible source but it is well within the region where PSF subtraction artifacts are large for stellar sources so it is difficult to rule out that it is a PSF subtraction artifact.

4.4. Q0850+440

This radio-quiet QSO has an associated absorption system at $z = 0.1638$. In an imaging and spectroscopic survey of faint galaxies, Lanzetta et al. (1995) reported a strong Ly- α absorption system and a possible indication of weak C IV absorption at $z = 0.1630$. They also obtained an unambiguous redshift of $z = 0.1635$ for a galaxy relatively close to the quasar sightline. The subsequent ultraviolet spectroscopic survey of Lanzetta et al. (1997) showed that the Ly- α absorption system at $z = 0.1638$ has $\log N(\text{H I}) = 19.8$. They concluded that this system is associated with a moderate-luminosity early-type galaxy, although it may actually arise in one of several very faint galaxies close to the QSO line of sight seen in their HST/WFPC2 images. These conclusions are supported by Chen et al. (2001) who confirmed the DLA system and the associated galaxy. Their photometric redshifts show that other galaxies in this field do not have the same redshift as the DLA system.

Four objects are identified in our H-band images. Object -9.04+1.53 is the galaxy designated as “G1” Lanzetta *et al.* (1997). We find it is a disk-like galaxy with a bulge-to-disk ratio of ~ 0.3 and scale lengths of $r_e \sim 0.7$ kpc and $r_d \sim 1.0$ kpc. Object -0.20-3.49 is the object designated “S1” Lanzetta *et al.* (1997). It is a point source in our images as well as the HST images of Lanzetta *et al.* (1997). Object +1.28+2.55 is a diffuse arm-like feature that can be seen in our H-band image as well as the HST images. The NIR emission appears to extend towards the quasar. We find an apparent H magnitude of 24.7 for this diffuse emission while Lanzetta *et al.* (1997) find an apparent AB magnitude of $m_{F702W} = 22.5$ mag. The F702W-H color of -2.2 is extremely blue. Object +0.56+0.32 is close to the line of sight to the quasar ($0.64''$) but we believe it to be real since we do not see a similar extension in the PSF subtracted stellar image (see Figure 1). In fact we see extended emission to the east of the quasar in each of the four techniques used to remove the quasar light contribution. In addition, the emission at +1.28+2.55 and at +0.56+0.32 appears to be continuous (Figure 5). We interpret the two emission features to be a single object with object +1.28+2.55 being an extension of the emission. We regard it as the likely absorber. If this is the correct interpretation, then the DLA is sampling a region very close ~ 2 kpc from the center of a

very blue galaxy. In addition, object -2.56+2.01, while identified as a separate object, is also very blue and could be part of this same emission. Object -2.56+2.01 is unresolved. We do not detect the object -00023+00043 identified in Lanzetta *et al.* (1997).

4.5. Q1127-145

PKS B1127-145 is a compact, gigahertz-peaked radio source at $z_{em} = 1.187$ with a jet seen in radio and X-ray images, and variability at radio wavelengths. Bergeron *et al.* (1991) identified Mg II, Fe II and Mg I absorption in the spectrum of the quasar at $z = 0.313$. They spectroscopically confirmed two late-type galaxies at the redshift of the absorber separated from the quasar by $9''.6$ and $17''.7$ and identified the closer one as the Mg II absorber. Lane *et al.* (1998) in a survey of H I 21-cm absorption in Mg II-selected systems using WSRT, discovered 21-cm absorption at $z = 0.3127$. HST/UV spectra show a damped Lyman- α profile with $N(\text{H I}) = (5.1 \pm 0.9) \times 10^{21} \text{ cm}^{-2}$ (Lane *et al.*, 1998; Rao & Turnshek, 2000). Lane *et al.* (1998) concluded that the galaxy which Bergeron *et al.* (1991) identified as the absorber, is unlikely to be the DLA system since its column density is unlikely to arise at the projected impact parameter ($\geq 20 \text{ kpc}$). Instead they suggested that the absorption comes from another galaxy with a separation $3''.9$ from the quasar, or from tidal debris associated with a group of galaxies. Bechtold *et al.* (2001) detected X-ray absorption with Chandra/ACIS, and suggested that the absorbing gas of the DLA has metallicity of 23% solar. Rao *et al.* (2003) identified the DLA galaxy as a patchy/irregular LSB structure which encompasses four objects. They suggest that the DLA system is more likely associated with the faintest object in the group found at the absorber redshift. Chen & Lanzetta (2003) also found that a group of at least four galaxies are at the redshift of the DLA and they concluded that because of the proximity of these galaxies to the QSO line of sight, it is difficult to separate the contribution of either of the galaxies to the DLA.

Six objects are identified in our image of this field. The angular distances of these objects to the QSO range from $0''.6$ to $16''$ corresponding to $b_{abs} = 2.5$ to 70 kpc . Object +8.86+3.98 corresponds to the object “G1” in Bergeron *et al.* (1991) at $9''.7$. Morphologically G1 appears to have both a disk and a bulge with a bulge-to-total ratio of ~ 0.4 . Tidal warping at the edge of this galaxy can be seen both in our H-band image and the HST F814W image. Our object -3.57+0.17 corresponds to the object identified as the likely absorber by (Lane *et al.* 1998).

Our image adds to the already crowded field of Q1127-145. We regard the object -0.13+0.57, appearing after PSF subtraction at an angular distance $0''.6$, as another candidate absorber simply due to its close proximity to the quasar line of sight. This object has not be

identified previously though the HST image has a shows a similar feature when the PSF is removed. We do not discount that the faint diffuse emission seen around the field could also contribute to the absorbing system but this close object would have an impact parameter of only ~ 2.5 kpc. It has not been reported previously but appears to extend at least one arcsecond away from the quasar. We do not detect all of the faint nebulosity seen in the immediate vicinity of the quasar in the HST images but have detected very diffuse emission extending NW $0''.5$ from the quasar.

4.6. Q1329+412

This radio-quiet QSO ($z_{em} = 1.93$) was observed by Sargent et al. (1988), who identified four distinct absorption redshifts in its spectrum. In a spectral survey of C IV absorption systems, they found a weak Mg II doublet at $z = 0.5009$. The IUE spectrum of this object shows a low-redshift candidate DLA system at $z = 0.5193$ with $\log N(H I) = 20.8$ (Lanzetta et al. 1995). HST/UV spectroscopy did not confirm the presence of this system (Turnshek et al. 2002) however subsequent HST spectra did reveal a DLA at the redshift ($z = 1.282$) of another Mg II system (Bechtold et al. 2002). Based on the equivalent width of the Ly α line at $z = 1.282$, the DLA system has a $\log N(H I) = 19.7$. There are additional metal-line systems at $z = 1.6012, 1.8355$ (C IV+Mg II), and $z = 1.4716, 1.9405$ (C IV).

Five objects are identified in our image of this field. The angular distances of these objects to the QSO range from $\Delta\theta = 2.4''$ to $6.5''$ corresponding to $b_{abs} = 20$ to 54 kpc at $z = 1.28$. There is no previous report of detection of these objects in the literature. Aragón-Salamanca et al. (1994) detected a faint object ($K \approx 19.75$) with an angular distance of $3''$ from the QSO line of sight, which could be object 1.81+2.04. Object -1.81+2.04 is evident in the HST F702W image. All objects are compact and faint. Objects -4.23+3.04 and +2.11-0.94 appear slightly extended; however, they would have impact parameters in excess of 20 kpc if they give rise to the absorption. We regard the likely absorber as the faint emission $0''.7$ south of the quasar. This object is evident in both our NIR image and in the HST image though we do not have the resolution or the signal-to-noise to determine its morphology.

5. SUMMARY AND FUTURE WORK

We present the first adaptive optics observations of low-redshift DLAs. The images have revealed several objects at close angular separations to the quasar in each field. The adaptive optics images are comparable to the HST images in resolution and several close

features are seen in common with HST and with these adaptive optics images. In addition, we report the detection of two previously unidentified objects in the fields of Q0738+313, where there are no HST images, and Q1127-145, where the HST detection is marginal.

The objects found around in these quasar absorption fields would be less than $0.1L_*$ if they are at the absorber redshift and most of the brighter objects appear to have disks. The census of the brighter objects in these six absorber fields is 6 disk-dominated galaxies, 3 disk+bulge galaxies, 2 bulge-dominated galaxies, 3 point sources, and 5 unconstrained objects. In addition, five of the six fields show objects between $0''.5$ and $1''.0$ to the line of sight to the quasar.

Our census has found likely candidates for all of the DLA systems. The KL subtraction reveals a candidate object just offset from the quasar line of sight in Q0054+144 though the HST field appears to have several faint objects distributed about the field. The DLA in Q0235+164 appears to be the object previously identified $1''$ East of the quasar (Yanny *et al.* 1989). In Q0738+313 we find a new object to which we attribute the lower-redshift DLA. This object would have an impact parameter of ~ 3 kpc. It appears to have emission extending several arcseconds to the NW. This emission could be associated with the jet and arm features identified by Turnshek *et al.* (2001) though this emission is fainter than the new object detected here. The DLA at $z = 0.22$ in this field has been previously identified. In Q0850+440 Lanzetta *et al.* (1995) find a dwarf galaxy $9''$ from the quasar ($b \sim 25$ kpc). We identify another object very close to the quasar line of sight as a candidate absorber. It appears only after subtraction of the quasar but if the absorption arises from this object, then the DLA arises close to the core of a very blue galaxy ($b \sim 2$ kpc). For Q1127-145 we find a faint diffuse object close to the line of sight of the quasar and extending NNW several arcseconds. The absorber in Q1329+412 is identified as arising from an object $0''.7$ south of the quasar. This object is also clearly seen in both our H-band image and an HST F702W image of the field.

All candidate absorbers are faint, with luminosities less than $0.1 L_H^*$ or $L_{K'}^*$. Assuming that at least some of these objects are at the same redshift as the absorbers, we conclude that the absorbers in our fields are associated with relatively low luminosity galaxies. Morphological analysis reveals that most of the brighter objects have a disk component. Their sizes, inferred from the surface brightness profiles, range from small to typical scale lengths for local disk galaxies. For reference, our Galaxy has a disk scale length of $r_d = 2.2$ kpc measured in the K -band (Maihara *et al.* 1978; Jones *et al.* 1981) and M31 has a scale length of $r_d = 3.9$ kpc in the K -band, and $r_d = 4$ kpc in the I -band (Hiromoto *et al.* 1983). Table 5 summarizes object morphologies and the derived linear impact parameter, luminosity, and scale lengths assuming the objects are at the redshift of the absorber.

Rao *et al.* (2003) have suggested that the DLAs at $z < 1$ are dominated by dwarf or low surface brightness galaxies. However, Chen and Lanzetta (2003), with more photometric redshifts, have suggested that the luminosity function of $z < 1$ DLAs could be much broader. Our observations, at higher resolution than both of these studies, have found all of the candidate absorbers to be faint, with significant disk components for the majority of the objects. This suggests that a considerable fraction of low- z DLAs may be faint, low surface brightness galaxies. Such a conclusion would appear to be consistent with the low metallicities found in low- z DLAs (e.g., Khare *et al.* (2004); Kulkarni *et al.* (2005); and references therein). However, it would be necessary to obtain redshift confirmations for our candidates and to obtain similar high-resolution images of other low- z DLAs to reach more definitive conclusions on the luminosity function of the absorber galaxies.

Our observations have demonstrated the use of adaptive optics for direct high-resolution imaging of the galaxies giving rise to quasar absorbers. Deeper observations of the same fields in the future with higher order AO systems would help to improve the signal-to-noise ratios in the fainter objects. Furthermore, adaptive optics systems with laser guide stars are not constrained by the need to have a bright guide star in the quasar field, and would thus be able to reach higher redshift absorbers.

It is crucial to also obtain spectroscopy (or at least narrow-band imaging) of all the fields to better constrain the redshifts of the detected candidate absorbers. With spectroscopic PSF subtraction procedures (such as those followed by Moller (2000)) it may be feasible to even verify the redshifts of the objects located very close to the line of sight of the quasar. It is essential to expand the sample of high-resolution broad-band images, followed with spectroscopic confirmations, for quasar absorbers at low and high redshifts. Such a combination of high-resolution imaging and spectroscopic observations of quasar absorbers can give direct information on their luminosities, sizes, and star formation rates and thus the nature of these galaxies. Performing such observations on different types of quasar absorbers (e.g., DLAs, weak Mg II systems, C IV systems) may help to understand any trends between the absorption line strengths and galaxy properties such as the luminosities and impact parameters. Finally, a comparison of these properties of quasar absorbers at low and high redshifts will allow us to study the evolution of the absorbing galaxies with cosmological time and the connection between the absorbers and the present-day galaxies.

This paper is based on observations obtained at the Gemini Observatory, which is operated by the Association of Universities for Research in Astronomy, Inc., under a cooperative agreement with the NSF on behalf of the Gemini partnership: the National Science Foundation (United States), the Particle Physics and Astronomy Research Council (United Kingdom), the National Research Council (Canada), CONICYT (Chile), the Australian Re-

search Council (Australia), CNPq (Brazil) and CONICET (Argentina). This paper is based on observations obtained with the Adaptive Optics System Hokupa'a/Quirc, developed and operated by the University of Hawaii Adaptive Optics Group, with support from the National Science Foundation. We thank the Gemini-North Observatory staff for assistance during our observations, Hsiao-Wen Chen for providing details of the published photometric data for Q1127-145, and B. Stobie of the University of Arizona for providing and assisting with the IDP-3 package. We also thank the referee of the paper for making a number of positive suggestions on the paper. VPK and SG gratefully acknowledge partial support from the National Science Foundation grant AST-0206197 and from the University of South Carolina Research Foundation. MT acknowledges support from National Science Foundation grant AST-0205960.

Facilities: Gemini-N(Hokupa'a).

REFERENCES

- Aragon-Salamanca, A., Ellis, R. S., Schwartzberg, J.-M., Bergeron, J. A. 1994, *ApJ*, 421, 27.
- Bahcall, J. N. et al. 1993, *ApJS*, 87, 1.
- Bahcall, J. N., Kirhakos, S., Schneider, D. P. 1996, *ApJ*, 457, 557.
- Bechtold, J., Siemiginowska, A., Aldcroft, T. L., Elvis, M., & Dobrzycki, A. 2001, *ApJ*, 562, 133.
- Bechtold, J., Dobrzycki, A., Wilden, B., Morita, M., Scott, J., Dobrzycka, D., Tran, K., and Aldcroft, T.L. 2002, *ApJS*, 140, 143.
- Bell, E. F., McIntosh, D. H., Katz, N., & Weinberg, M. D. 2003, *ApJS*, 149, 289.
- Bergeron, J., Boisse, P. 1991, *A&A*, 243, 344.
- Bertin, R., & Arnouts, S. 1996, *A&AS*, 117, 393.
- Bessell 1979, *PASP*, 91, 589.
- Bolzonella, M., Miralles, J.-M., Pella, R. 2000, *A&A*, 363, 476.
- Bowen, D. V., Tripp, T. M., & Jenkins, E. B. 2001, *AJ*, 121, 1456.
- Bruzual G., Charlot, S. 1993, *ApJ*, 405, 538.

- Burbidge, E. M., Beaver, E. A., Cohen, R. D., Junkkarinen, V. T., Lyons, R. W. 1996, *AJ*, 112, 2533.
- Chen, H. W., Lanzetta, K. M., Webb, J. K., & Barcons, X. 1998, *ApJ*, 498, 77.
- Chen, H.-W., & Lanzetta, K. M. 2003, *ApJ*, 597, 706.
- Chen, H.-W., Lanzetta, K. M., Webb, J. K., Barcons, X. 2001, *ApJ*, 559, 654.
- Chengalur, J. N., Kanekar, N. 1999, *MNRAS*, 302, 29.
- Chun, M. 1998, *PASP*, 110, 317.
- Cohen, J. G. 2001, *AJ*, 121, 1275.
- Cohen, R. D., Burbidge, E. M., Junkkarinen, V. T., Lyons, R. W., & Majejski, G. 1999, *BAAS*, 194, 71.01
- de Jong, R. S., Simard, L., Davies, R. L., Saglia, R. P., Burstein, D., Colless, M., McMahan, R., and Wegner, G. 2004, *MNRAS*, 355, 1155.
- Djorgovski, S. G., Pahre, M. A., Bechtold, J., & Elston, R. 1996, *Nature*, 382, 234.
- Drinkwater, M. J., Webster, R. L., & Thomas, P. A. 1993, *AJ*, 106, 848.
- Fynbo, J. U., Moller, P., and Thomsen, B. 2001, *A&A*, 368, 408
- Gavazzi, G., Franzetti, P., Boselli, A., Pierini, D., Scodreggio, M. 2000, *A&A*, 361, 863.
- Gavazzi, G., Zibetti, S., Boselli, A., Franzetti, P., Scodreggio, M., and Martoochi, S. 2001, *A&A*, 372, 24.
- Graves, J. Elon et al. 2000, *SPIE*, 4007, 26.
- Haehnelt, M., Steinmetz, M., Rauch, M. 1998, *ApJ*, 495, 647.
- Hiromoto, N., Maihara, T., Oda, N., and Okuda, H. 1983, *PASJ*, 35, 413
- Hodapp, K., et al. 1996 *NewA*, 1, 177.
- Hunstead, R. W., Pettini, M., & Fletcher, A. B. 1990, *ApJ*, 365, 23.
- Jimenez, R., Bowen, D. V., & Matteucci, F. 1999, *ApJ*, 514, L83.
- Jones, T.J., Ashley, M., Hyland, A. R., and Ruelas–Mayorga, A. 1981, *MNRAS*, 197, 413.

- Junkkarinen, V. T., Cohen, R. D., Beaver, E. A., Burbidge, E. M., Lyons, R. W., & Madejski, G. 2004, *ApJ*, 614, 658.
- Khare, P., Kulkarni, V. P., Lauroesch, J. T., York, D. G., Crofts, A. P. S., & Nakamura, O. 2004, *ApJ*, 616, 86.
- Kirhakos, S., Sargent, W. L. W., Schneider, D. P., Bahcall, J. N., Jannuzi, B. T., Maoz, D., & Small, T. A. 1994, *PASP*, 106, 646.
- Kron, R. G. 1980, *ApJS* 43 305.
- Kulkarni, V. P., Hill, J. M., Weymann, R. J., Storrie-Lombardi, L. J., Rieke, M. J., Schneider, G., Thompson, R. I., & Jannuzi, B. 2000, *ApJ*, 536, 36
- Kulkarni, V. P., Hill, J. M., Schneider, G., Weymann, R. J., Storrie-Lombardi, L. J., Rieke, M. J., Thompson, R. I., & Jannuzi, B. 2001, *ApJ*, 551, 37.
- Kulkarni, V. P., Fall, S. M., Lauroesch, J. T., York, D. G., Welty, D. E., Khare, P., & Truran, J. W. 2005, *ApJ*, 618, 68.
- Lanzetta, K. M., Wolfe, A. M., Turnshek, D. A. 1995, *ApJ*, 440, 435.
- Lanzetta, K. M., Wolfe, A. M., Altan, H., Barcons, X., Chen, H. W., Fernandez-Soto, A., Meyer, D. M., Ortiz-Gil, A., Savaglio, S., Webb, J. K., & Yahata, N. 1997, *AJ*, 114, 1337.
- Lane, W., Smette, A., Briggs, F., Rao, S., Turnshek D., & Meylan, G. 1998, *AJ*, 116, 26.
- Lauer, T. 2002, *Proceedings of the SPIE*, 4847, 167.
- Le Brun, V., Bergeron, J., Boisse, P., & Deharveng, J. M. 1997, *A&A*, 321, 733.
- Lowenthal, J. D., Hogan, C. J., Green, R. F., Woodgate, B. E., Caulet, A., Brown, L., & Bechtold, J. 1995, *ApJ*, 451, 484
- Lupton, R. H., J. E. Gunn, Z. Ivevic, G. R. Knapp, S. Kent, and N. Yasuda 2001, *Astron. Soc. Pac. Conf. Proc.*, 238, 269.
- Lytle, D., Stobie, E., Ferro, A., & Barg, I., 1999, *ASP Conf. Ser.* 172, *Astronomical Analysis Software and Systems 8*, ed. D. Mehringer, R. Plante & D. Roberts (San Francisco: AP), 445
- Maihara, T., Oda, N., Sugiyama, T. and Okuda, H. 1978, *PASJ*, 30, 1.

- Maller, A. H., Prochaska, J. X., Somerville, R. S., Primack, J. R. 2001, MNRAS, 326, 1475.
- Marquez, I., Petitjean, P., Theodore, B., Bremer, M., Monnet, G., Beuzit, J.-L. 2001, A&A, 371, 97.
- Matteucci, F. Molaro, P. & Vladilo, G. 1997, A&A, 321, 45.
- McLure, R. J., Kukula, M. J., Dunlop, J. S., Baum, S. A., O’Dea, C. P., Hughes, D. H. 1999, MNRAS, 308, 377.
- McDonald, P., & Miralda-Escud’e, J. 1999, ApJ, 519, 486
- Moller, P. 2000, Msngr, 99, 31.
- Oke, J. B., & Gunn, J. E. 1983, ApJ, 266, 713.
- Peng, C., Ho, L., Impey, C. & Rix, H. 2002, AJ, 124, 266
- Peroux, C., McMahon, R. G., Storrie-Lombardi, M. J., & Irwin, M. J. 2003, MNRAS, 346, 1103.
- Prochaska, J. X., & Wolfe, A. M. 1997, ApJ, 487, 73.
- Prochaska, J. X., & Wolfe, A. M. 1998, ApJ, 507, 113.
- Rao, S. M., & Turnshek, D. A. 1998, ApJ, 500, L115
- Rao, S. M., & Turnshek, D. A. 2000, ApJS, 130, 1
- Rao, S. M., Nestor, D. B., Turnshek, D. A., Lane, W. M., Monier, E. M., & Bergeron, J. 2003, ApJ, 595, 94.
- Rigaut, F. 2005, private communication.
- Roberts, M. S., Brown, R. L., Brundage, W. D., Rots, A. H., Haynes, M. P., Wolfe, A. M. 1976, AJ, 81, 293.
- Rosenberg, J. L., & Schneider, S. E. 2003, ApJ, 585, 256.
- Sargent, W. L. W., Steidel, C. C., Boksenberg, A. 1988, ApJS, 68, 539.
- Siemiginowska, A., Bechtold, J., Aldcroft, T. L., Elvis, M., Harris, D. E., & Dobrzycki, A. 2002, ApJ, 570, 543.
- Simard, L., Willmer, C. N. A., Vogt, N. P., Sarajedini, V.L., Phillips, A.C., Weiner, B.J., Koo, D.C., Im, M., Illingworth, G. D., and Faber, S. M., 2002 ApJS, 142, 1.

- Smith, H. E., Junkkarinen, V. T., Burbidge, E. M 1977, ApJ, 218, 611.
- Smith, H. E., Cohen, R. D., Burns, J. E., Moore, D. J., & Uchida, B. A. 1989, ApJ, 347, 87.
- Steidel, C. C., Pettini, M., Dickinson, M., & Persson, S. E. 1994, AJ, 108, 2046.
- Steidel, C. C., Bowen D. V., Blades, J. C., & Dickinson, M. 1995, ApJ, 440, L45
- Steidel, C. C., Kollmeier, J. A., Shapley, A. E., Churchill, C. W., Dickinson, M., & Pettini, M. 2002, ApJ, 570, 526.
- Tokunaga, A. T. 1999, in Allen’s Astrophysical Quantities, ed. Arthur N. Cox (New York: Springer), 143.
- Turnshek D. A., Rao, S., Nestor, D., Lane, W., Monier, E., Bergeron, J., & Smette, A. 2001, ApJ, 553, 288.
- Turnshek, D. A., Rao, S. M. 2002, ApJ, 572, 7.
- Wainscoat, R. J., & Cowie, L. L. 1992, AJ, 103, 332
- Wolfe, A. M., Turnshek, D. A., Smith, L. J., & Cohen, R. D. 1986, ApJS, 61, 249.
- Wolfe, A. M., Lanzetta, K. M., Foltz, C. B., & Chaffee, F. H. 1995, ApJ, 454, 698.
- Wolfe, A. M., Prochaska, J. X. 1998, ApJ, 494, 15.
- Yanny, B., York, D. G., Gallagher, J. S. 1989, ApJ, 338, 735.
- York, D. G., Dopita, M., Green, R., & Bechtold, J. 1986, ApJ, 311, 610.
- York, D. G., Yanny, B., Crotts, A., Carilli, C., Garrison, E., Matheson, L. 1991, MNRAS, 250, 24.

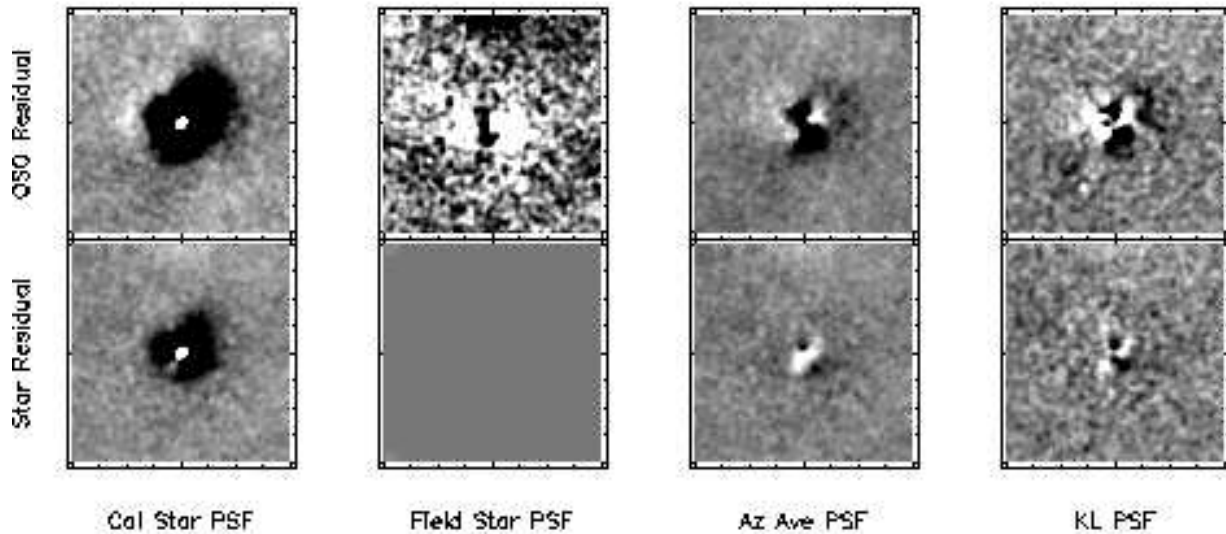


Fig. 1.— A comparison of the four techniques used to remove the contribution of the quasar light to the image within the $4'' \times 4''$ region centered on the quasar. The axes are marked with $0.5''$ intervals. Each column shows one of the techniques applied to the quasar (top) and a star (bottom) in the field of Q0850+400. The left most column shows the residual in the quasar/star images when the PSF is constructed from the PSF calibration observations. The second column shows the residuals when the PSF is constructed from the star within the field. The field star residual image is by definition zero. The third column shows the residuals when the PSF is constructed from the azimuthal average of the quasar image. The last column shows the residual when the PSF is modeled as a fit of the first 30 modes of the Karhunen-Loeve (KL) basis calculated from the sequence of individual quasar exposures in the observation. Residuals in the KL PSF stellar image subtraction extend to a radius of about $0''.5$. In all cases, the PSF was scaled and translated to minimize the variance within the $4'' \times 4''$ images. All images are displayed with the maximum and minimum intensities scaled to the sky $\pm 0.1\%$ of the peak intensity in the unsubtracted images. The residual images have been smoothed by a gaussian with FWHM=3 pixels.

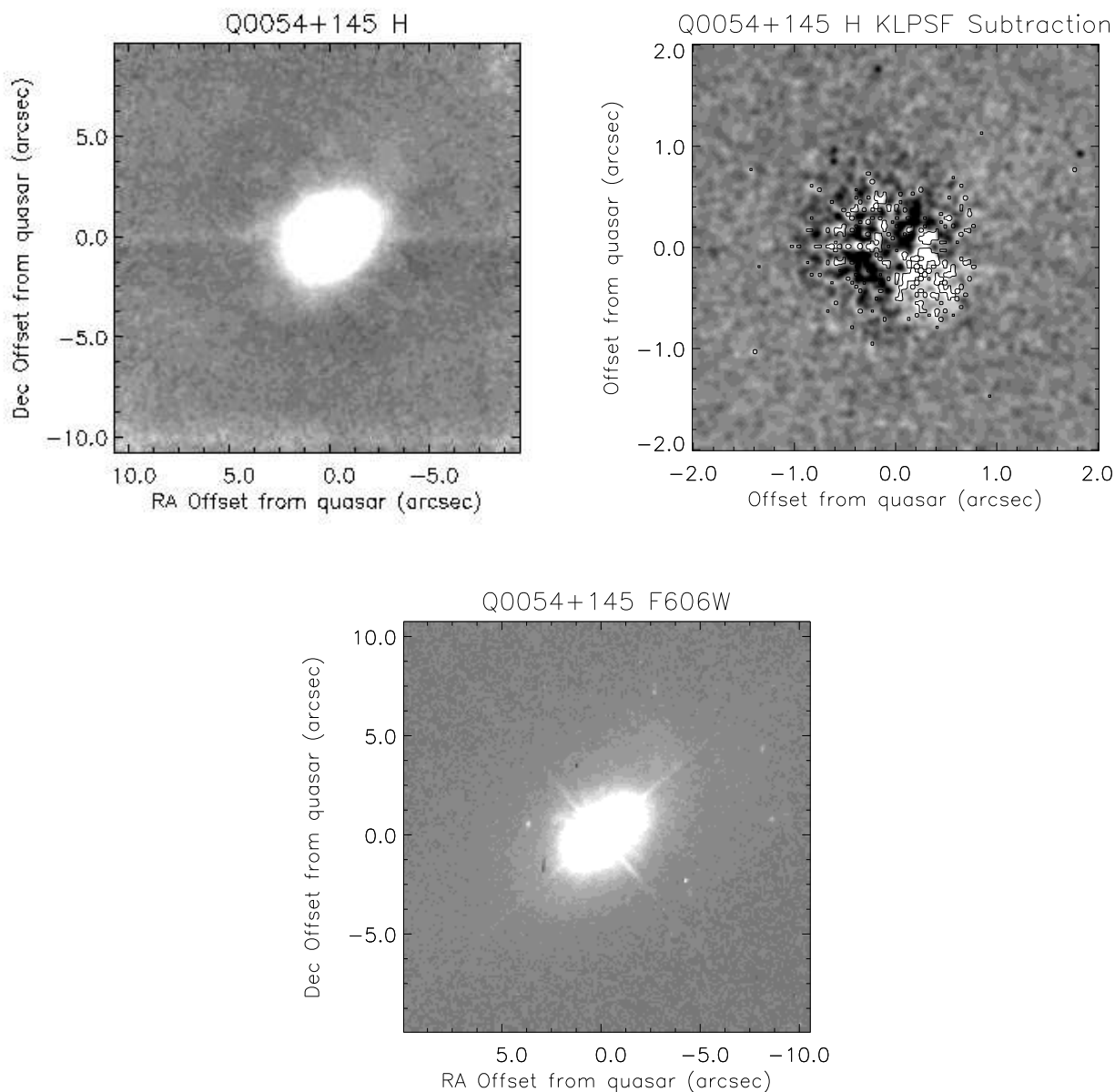


Fig. 2.— Upper left panel shows our Gemini/Hokupaa H-band image smoothed by a gaussian with FWHM=0".2. The upper-right panel shows the quasar subtracted image of the central 4'' smoothed by a 3-pixel gaussian. Contours are overlaid on the image at 3σ above the sky in the unsmoothed image. The bottom panel shows the HST/WPFC2 F606W image. All figures are shown in a linear intensity scale with North up and East to the left. The linear E-W feature running across the upper-left image is an artifact caused by the detector quadrant boundary.

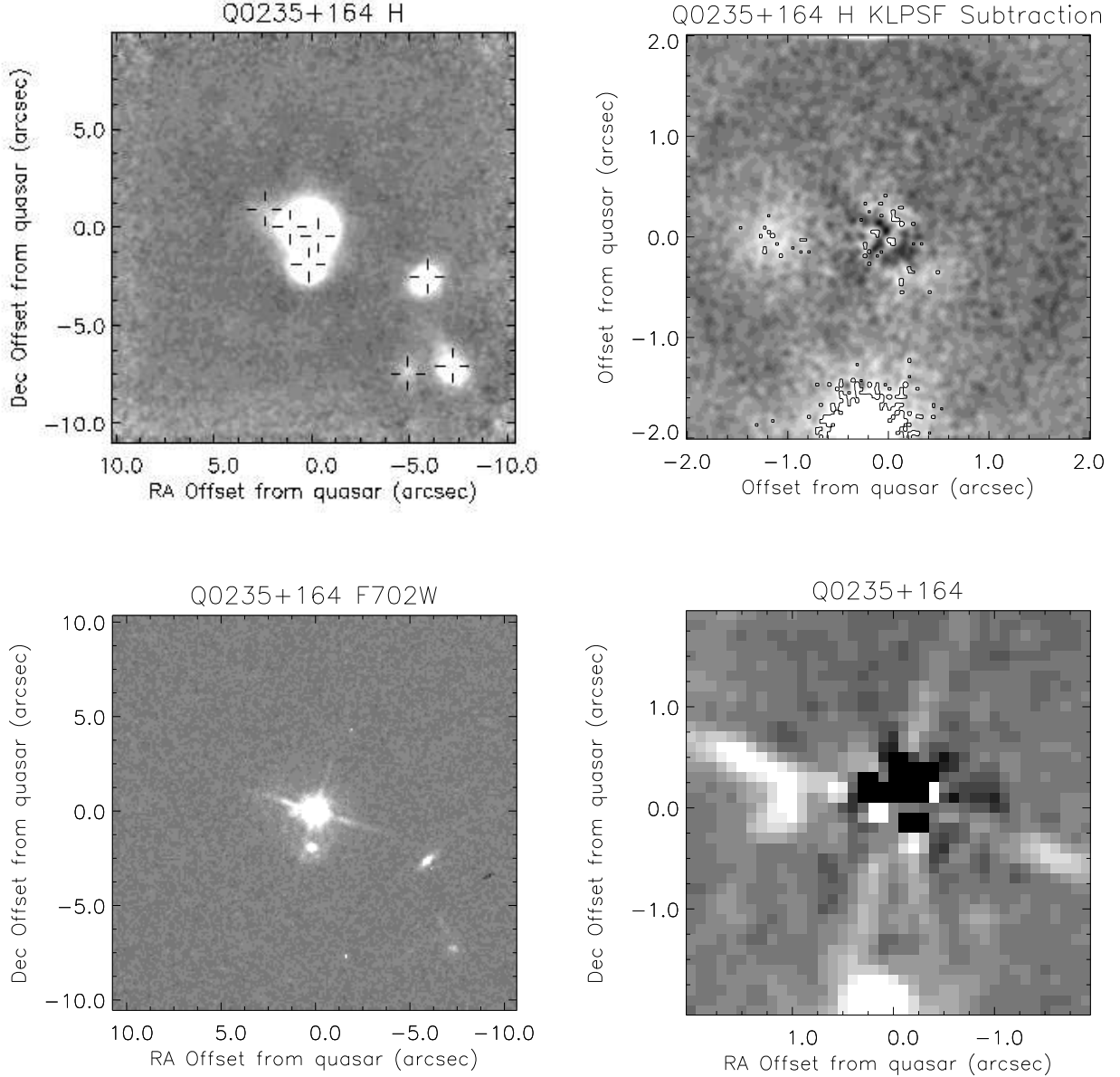


Fig. 3.— Upper left panel shows our Gemini/Hokupa’a H-band image smoothed by a gaussian of $\text{FWHM}=0\farcs2$. The upper-right panel shows our Quasar-subtracted H-band image of the central $4\farcs$ smoothed by a 3-pixel gaussian. Contours overlaid on this image are 3σ above the sky in the unsmoothed image. Lower panels shows the HST/WPC2 F702W image for comparison. The lower-left panel shows the HST image corresponding to our full H-band image while the lower-right panel shows the azimuthal-average PSF subtracted HST image. All figures are shown with a linear intensity scale with North up and East to the left. We identify object $+1.11-0.01$ as the most likely candidate absorber. This object has been previously identified as a candidate absorber (e.g. object A1 in (Yanny *et al.* 1989)). The object seen $2\farcs$ south of the quasar is the BALQSO object (Object “A” identified by (Burbidge *et al.* 1996)). There is a small extension SW of the center of the field but it is too close to the center of the field to be distinguished from residuals of the quasar subtraction.

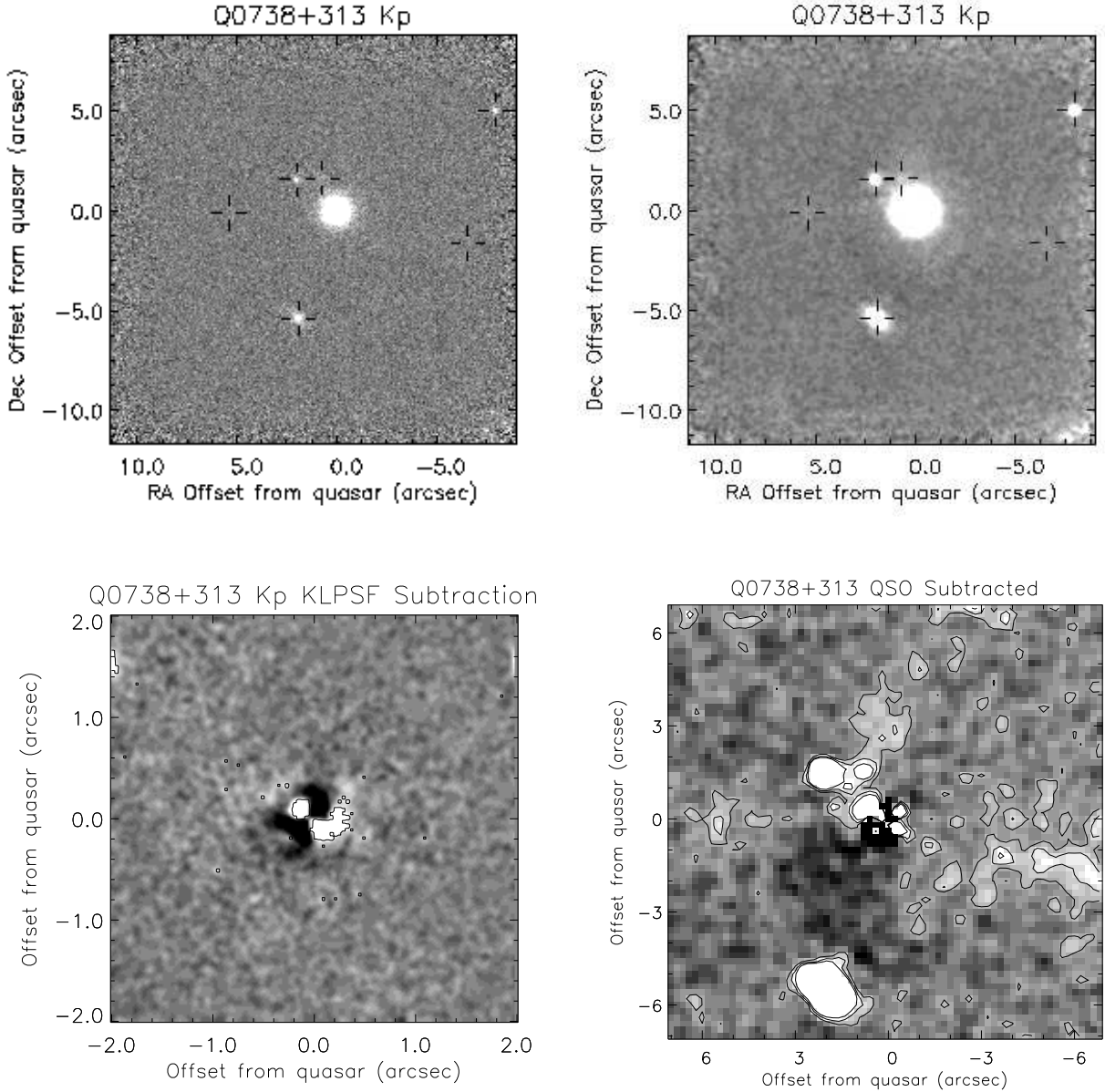


Fig. 4.— Upper panels show our Gemini/Hokupa’a K' image of Q0738+313 unsmoothed (left) and smoothed (right) by a gaussian with $\text{FWHM}=0''.2$. The full image in the top two panels are $20''$ on a side corresponding to 30 kpc at $z = 0.0912$ and 70 kpc at $z = 0.2212$. The lower-left panel shows the KL QSO-subtracted image. The lower-right figure shows the K' image after smoothing by a gaussian with FWHM equal to twice the FWHM of the quasar image, subtracting an azimuthal averaged PSF, and then binning the image to $0.2''$ pixels. The image shows the $14'' \times 14''$ region centered on the location of the quasar. The contours are 1-, 2- and 3-sigma above the sky in the smoothed-rebinned image. The one-sigma per pixel level corresponds to $22.3 \text{ mag arcsec}^{-2}$. The ‘jet’ and ‘arm’ reported by Turnshek *et al.* (2001) are apparent as are new features NNE of the subtracted quasar.

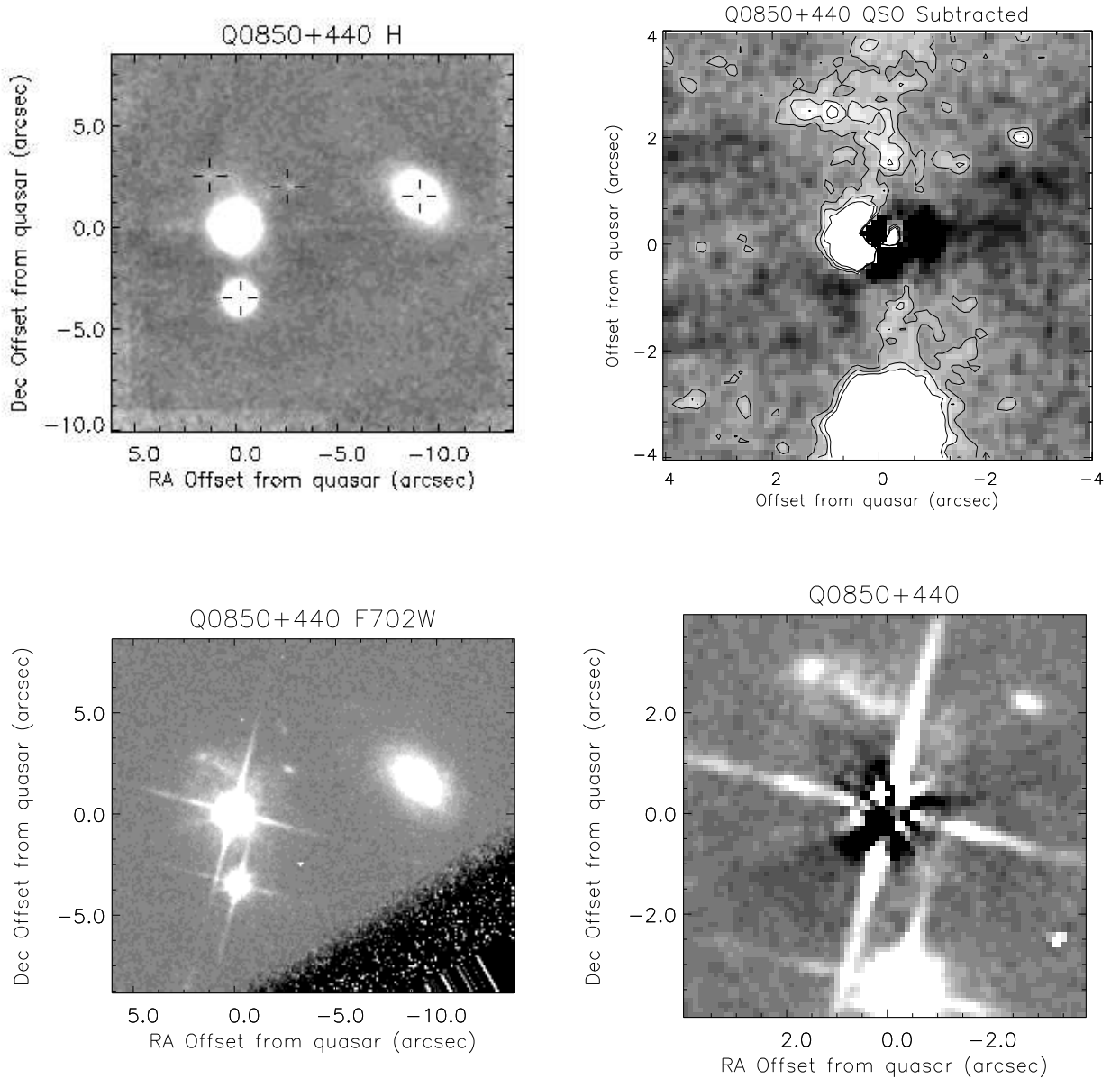


Fig. 5.— The upper panels show our H-band images of the field around the quasar before and after subtraction of the PSF image. The full image (upper-left) corresponds to ≈ 54 kpc at $z = 0.1638$. We found objects close to the line of sight to the quasar with several arcsecond extensions. The extent of the emission is shown in the $8'' \times 8''$ region centered on the azimuthal-average QSO-subtracted image (upper-right). This image was smoothed by a gaussian with $\text{FWHM}=0''.2$. The contours are 1-, 2- and 3-sigma above the sky in the smoothed-rebinned image. The lower panels show the HST F702W image (left) and its azimuthal-averaged subtracted image (right).

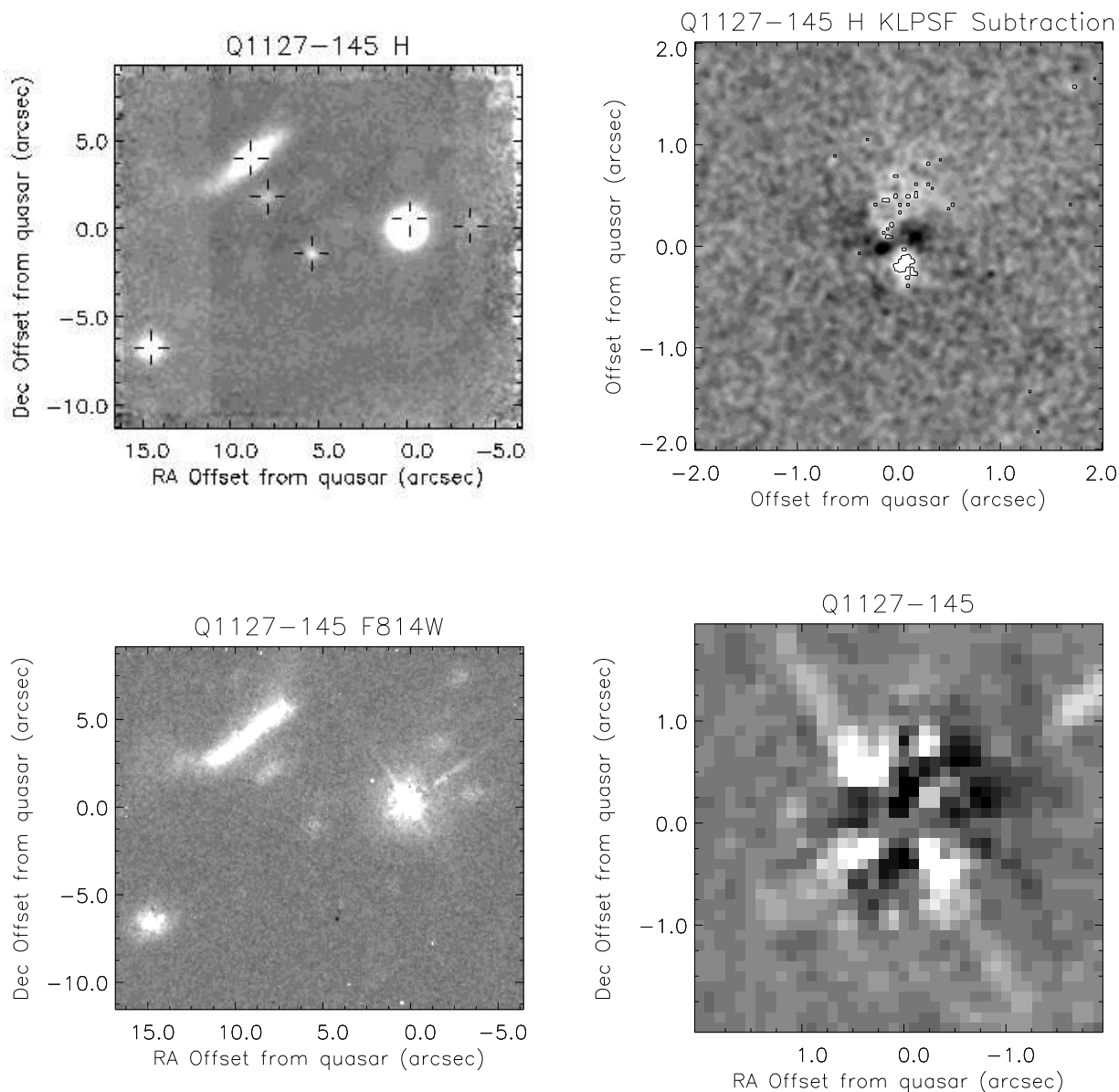


Fig. 6.— The upper panels show our image of the field before (left) and after (right) subtraction of the QSO image. The upper-left image is $23'' \times 20''$ corresponding to $\approx 100 \times 88$ kpc² at $z = 0.3127$. Five of the objects can be seen in the full frame image. The sixth object $-00.09+00.45$, just north of the quasar, is only seen after the PSF subtraction. The emission to the south of the quasar is not considered since it is less than $0''.5$ from the quasar.

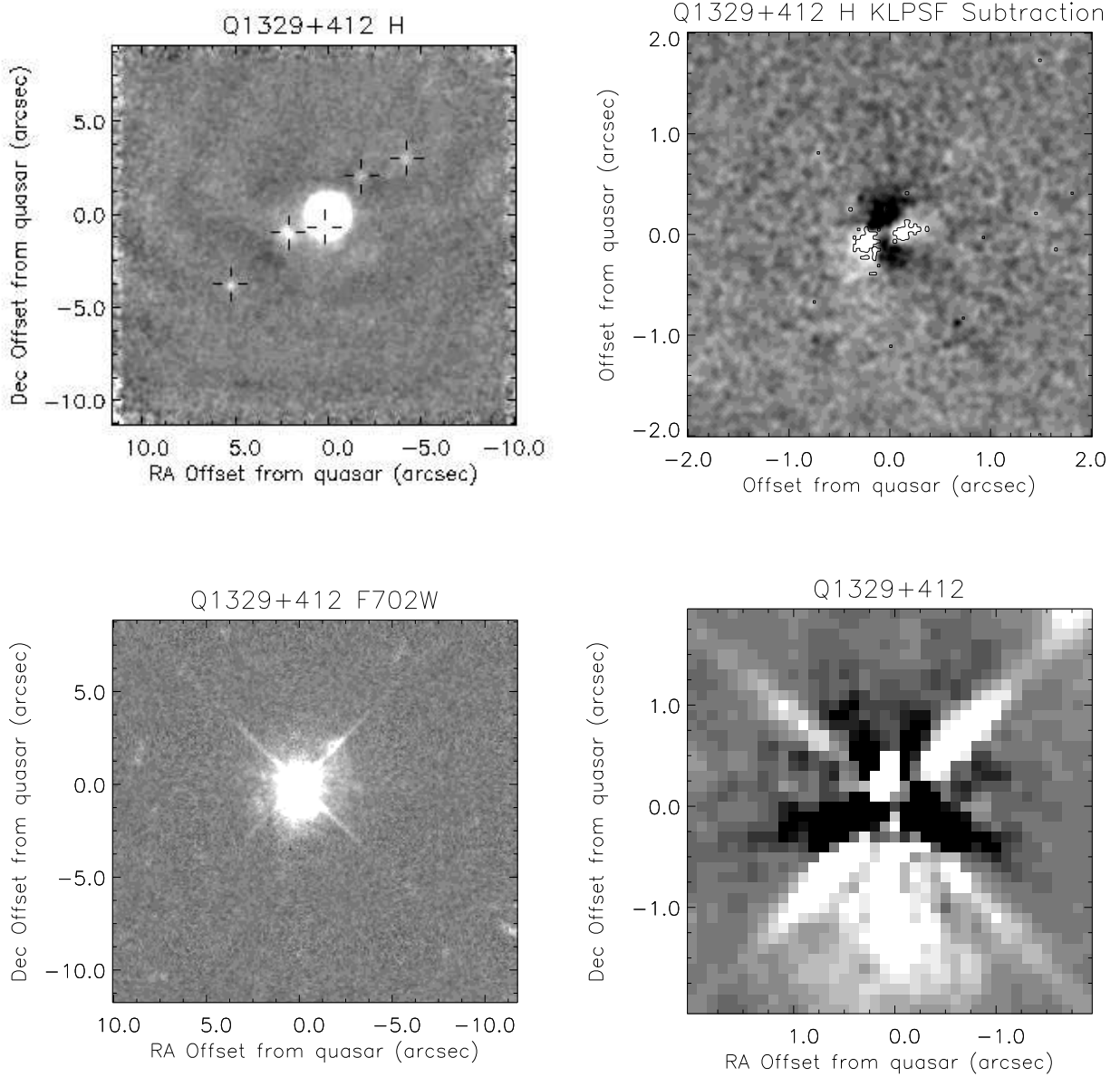


Fig. 7.— The upper left and right panels show our image of Q1329+412 before and after QSO subtraction. The full image (left) is $27.1'' \times 20''$ corresponding to $\approx 190 \times 165 \text{ kpc}^2$ at $z = 1.28$. Four objects found by SExtractor are clearly seen in the full frame H-band image. Object $-01.79+02.02$ is also evident in the HST F702W image NW of the quasar (lower right panel). The H-band and HST QSO-subtracted images show similar residual emission. SExtractor identifies a fifth object $+0.20-0.69$ in the KL QSO subtracted H-band image. This may correspond to the emission seen south of the quasar in the HST image.

Table 1. Target Properties

QSO	V	z_{em}	z_{abs}	$\log N(\text{H I})$	Absorber type	N(H I) Reference ^a
Q0054+144	16.1	0.171	0.103	18.3	Lyman-limit	1, 2
Q0235+164	15.5-19	0.940	0.524	21.65	DLA	3
Q0738+313	16.1	0.635	0.0912	21.18	DLA	4, 5
Q0738+313	16.1	0.635	0.2212	20.90	DLA	4, 6
Q0850+440	16.4	0.5139	0.1638	19.81	sub-DLA	7
Q1127-145	16.9	1.184	0.3127	21.7	DLA	3
Q1329+412	16.3	1.9300	1.282	19.7	sub-DLA	8

^aReferences: 1. Lanzetta et al. (1995); 2. Turnshek et al. (2002); 3. Junkkarinen et al. (2004); 4. Rao & Turnshek (1998); 5. Chengalur & Kanekar (1999); 6. Lane et al. (1998); 7. Lanzetta et al. (1997).; 8. Bechtold et al. (2002);

Table 2. Summary of Observations

QSO	Filter	Total Integration Time seconds	FWHM ^a arcsec	50%-EED ^a arcsec	$1\sigma \mu_{lim}^b$ mag/arcsec ²	$3\sigma m_{lim}^c$ mag
Q0054+144	H	23×120	0.46	0.75	19.6	21.9
Q0235+164	H	53×120	0.50	0.82	19.9	22.2
Q0738+313	K'	74×60	0.19	0.28	18.9	21.2
Q0850+440	H	39×120	0.23	0.38	20.0	22.3
Q1127-145	H	32×180	0.33	0.54	20.0	22.3
Q1329+412	H	48×180	0.29	0.47	20.1	22.4

^aFWHM and 50% EED measured from the QSO.

^b 1σ per pixel limit

^c 3σ limit within 75 pixels

Table 3. Summary of Objects Detected

QSO	Object $\Delta\alpha(^{\prime\prime})\Delta\delta(^{\prime\prime})$	$\Delta\theta(^{\prime\prime})$	m(AB)
Q0054+145	QSO	0	$H = 14.6$
	-0.29-0.74	0.79	21.5
Q0235+164	QSO	0	$H = 16.7^{\dagger}$
	-0.33-0.45	0.56	23.9 [†]
	+1.11-0.01	1.11	21.9 [†]
	+0.15-1.91	1.92	20.2 [†]
	+2.40+0.93	2.57	24.9 [†]
	-5.85-2.69	6.44	20.3 [†]
	-4.93-7.47	8.95	24.3 [†]
-7.15-7.21	10.15	20.6 [†]	
Q0738+313	QSO	0	$K' = 16.1$
	+0.71+1.63	1.78	22.6 ^a
	+2.02+1.54	2.54	21.3
	+5.40-0.11	5.40	23.0 ^a
	+1.90-5.38	5.71	19.8
	-6.58-1.64	6.78	22.4 ^{a,b}
	-7.96+5.02	9.41	21.4
Q0850+440	QSO	0	$H = 15.8$
	+0.56+0.32	0.64	...
	+1.28+2.55	2.85	24.7 ^c
	-2.56+2.01	3.25	25.8 ^c
	-0.20-3.49	3.50	17.6
	-9.04+1.53	9.17	17.8
Q1127-145	QSO	0	$H = 16.5$
	-0.13+0.57	0.58	...
	-3.57+0.17	3.57	24.6 ^d
	+5.42-1.40	5.60	22.6

Table 3—Continued

QSO	Object $\Delta\alpha(^{\prime\prime})\Delta\delta(^{\prime\prime})$	$\Delta\theta(^{\prime\prime})$	m(AB)
	+7.92+1.82	8.13	23.8
	+8.86+3.98	9.71	18.5
	+14.49-6.76	16.0	19.9
Q1329+412	QSO	0	$H = 17.0$
	+0.20-0.69	0.72	...
	+2.11-0.94	2.31	22.5
	-1.81+2.04	2.73	25.7 ^c
	-4.23+3.04	5.21	24.6 ^e
	+5.23-3.76	6.44	24.9

[†]Observations were nonphotometric for 0235+164. Magnitudes are given only for relative photometry.

^aThese objects are only detected after the image was heavily smoothed by a gaussian FWHM=0".2. The detections are $\geq 3\sigma$ /pixel in the smoothed image. Object +5.40-0.11 corresponds to the Turnshek *et al.* (2001) "arm" while object -6.58-1.64 corresponds to their "jet".

^bSExtractor also found an object at -1.38-0.76. This object has a magnitude of 24.7. We have combined it the linear feature listed here.

^cDetected with 75 pixels, 0.9σ /pixel threshold

^dCombined three close detections

^eDetected with 75 pixels, 0.8σ /pixel threshold

Table 4. Morphological Parameters

QSO	Obj	B/T	$r_{1/n}$ ($''$)	r_d ($''$)	n
Q0235+164	+1.11 – 0.01	$0.50^{+0.50}_{-0.50}$	$0.00^{+0.01}_{-0.00}$	$0.05^{+0.01}_{-0.05}$	$3.29^{+2.09}_{-1.88}$
	+0.15 – 1.91	$0.27^{+0.03}_{-0.03}$	$0.00^{+0.00}_{-0.00}$	$0.21^{+0.00}_{-0.01}$	$5.02^{+0.30}_{-0.31}$
	–5.85 – 2.69	$0.26^{+0.08}_{-0.08}$	$0.02^{+0.02}_{-0.02}$	$0.20^{+0.02}_{-0.02}$	$5.21^{+0.55}_{-0.35}$
	–4.93 – 7.47	$0.20^{+0.58}_{-0.20}$	$0.09^{+0.18}_{-0.09}$	$0.10^{+0.18}_{-0.07}$	$3.49^{+0.40}_{-0.20}$
	–7.15 – 7.21	$0.91^{+0.09}_{-0.14}$	$0.33^{+0.09}_{-0.08}$	$0.33^{+0.09}_{-0.32}$	$3.81^{+0.67}_{-0.90}$
Q0738+313	+2.02 + 1.54	$1.00^{+0.00}_{-0.70}$	$0.00^{+0.00}_{-0.00}$	$0.01^{+0.00}_{-0.00}$	$7.32^{+2.68}_{-2.47}$
	+1.90 – 5.38	$0.34^{+0.11}_{-0.11}$	$0.03^{+0.02}_{-0.02}$	$0.15^{+0.02}_{-0.02}$	$3.32^{+0.24}_{-0.20}$
	–7.96 + 5.02	$0.68^{+0.32}_{-0.68}$	$0.00^{+0.01}_{-0.00}$	$0.00^{+0.01}_{-0.00}$	$7.38^{+2.62}_{-2.93}$
Q0850+440	–2.56 + 2.01	$0.11^{+0.21}_{-0.11}$	$0.01^{+0.08}_{-0.01}$	$0.22^{+0.08}_{-0.10}$	$3.70^{+1.30}_{-0.79}$
	–0.20 – 3.49	$0.00^{+0.00}_{-0.00}$	$0.10^{+0.00}_{-0.00}$	$0.00^{+0.00}_{-0.00}$	$3.94^{+0.00}_{-0.01}$
	–9.04 + 1.53	$0.24^{+0.01}_{-0.01}$	$0.24^{+0.01}_{-0.01}$	$0.40^{+0.01}_{-0.00}$	$3.69^{+0.09}_{-0.08}$
Q1127-145	+5.42 – 1.40	$0.96^{+0.04}_{-0.39}$	$0.11^{+0.18}_{-0.06}$	$0.00^{+0.18}_{-0.00}$	$3.93^{+1.25}_{-1.13}$
	+7.92 + 1.82	$0.57^{+0.43}_{-0.57}$	$0.12^{+0.12}_{-0.12}$	$0.32^{+0.12}_{-0.22}$	$4.25^{+1.29}_{-1.44}$
	+8.86 + 3.98	$0.36^{+0.02}_{-0.03}$	$0.22^{+0.01}_{-0.04}$	$0.88^{+0.01}_{-0.07}$	$4.09^{+0.11}_{-0.21}$
	+14.5 – 6.76	$0.19^{+0.10}_{-0.07}$	$0.02^{+0.10}_{-0.02}$	$0.22^{+0.10}_{-0.02}$	$3.99^{+0.36}_{-0.49}$
Q1329+412	+2.11 – 0.94	$0.16^{+0.11}_{-0.09}$	$1.76^{+1.15}_{-0.81}$	$3.52^{+1.15}_{-0.02}$	$4.91^{+0.20}_{-0.10}$
	–1.81 + 2.04	$0.56^{+0.44}_{-0.56}$	$0.00^{+0.00}_{-0.00}$	$0.27^{+0.00}_{-0.16}$	$2.41^{+1.84}_{-1.24}$
	–4.23 + 3.04	$0.87^{+0.13}_{-0.75}$	$0.06^{+0.15}_{-0.06}$	$0.30^{+0.15}_{-0.15}$	$5.78^{+0.62}_{-0.85}$
	+5.23 – 3.76	$0.64^{+0.36}_{-0.64}$	$0.01^{+0.03}_{-0.01}$	$0.16^{+0.03}_{-0.16}$	$4.64^{+1.12}_{-1.04}$

Table 5. Summary of Derived Quantities of Objects Detected

QSO	Obj	$b_{\text{abs}}^{\text{a}}$ [kpc]	$\log(L/L_*)^{\text{b}}$	Morphology ^c	$r_{1/n}^{\text{d}}$ [kpc]	r_d^{d} [kpc]
Q0054+145	-0.29-0.74	1.40				
Q0235+164 ^e	-0.33-0.45	3.36				
	+1.11-0.01	6.66			0.0	0.3
	+0.15-1.91	11.53		B+D	0.0	1.3
	+2.40+0.93	15.43				
	-5.85-2.69	38.66		Dd	0.1	1.2
	-4.93-7.47	53.73			0.5	0.6
	-7.15-7.21	60.93		B	2.0	2.0
Q0738+313 ^f	+0.71+1.63	2.90 6.09	-2.32 -1.48			
	+2.02+1.54	4.14 8.69	-1.80 -0.96	P	0.0 0.0	0.0 0.0
	+5.40-0.11	8.80 18.48	-2.48 -1.64			
	+1.90-5.38	9.31 19.54	-1.20 -0.36	D+B	0.1 0.1	0.2 0.5
	-6.58-1.64	11.05 23.21	-2.24 -1.40			
	-7.96+5.02	15.34 32.21	-1.84 -1.00	P	0.0 0.0	0.0 0.0
Q0850+440	+0.56+0.32	1.77				
	+1.28+2.55	7.69	-4.09			
	-2.56+2.01	8.77	-4.53	D	0.0	0.6
	-0.20-3.49	9.44	-1.25	P	0.3	0.0
	-9.04+1.53	24.74	-1.33	D	0.7	1.1
Q1127-145	-0.13+0.57	2.55				
	-3.57+0.17	15.70	-3.42			
	+5.42-1.40	24.63	-2.62		0.5	0.0
	+7.92+1.82	35.75	-3.10		0.5	1.4
	+8.86+3.98	42.70	-0.98		1.0	3.9
	+14.49-6.76	70.32			0.1	1.0

Table 5—Continued

QSO	Obj	$b_{\text{abs}}^{\text{a}}$ [kpc]	$\log(L/L_*)^{\text{b}}$	Morphology ^c	$r_{1/n}^{\text{d}}$ [kpc]	r_d^{d} [kpc]
Q1329+412 ^g	+0.20-0.69	4.30				
	+2.11-0.94	13.80	-2.06	D	10.	21.
	-1.81+2.04	16.31	-3.34		0.0	1.6
	-4.23+3.04	31.13	-2.90		0.4	1.8
	+5.23-3.76	38.48	-3.02		0.1	1.0

^aProjected impact parameter in units of h^{-1} kpc, assuming the object to be at the absorber redshift with $h = 0.73$. In the case of Q0738+313, the two numbers given correspond to the two absorbers at $z = 0.0912$ and $z = 0.2212$, respectively.

^bThe object luminosities assume the objects are at the absorber redshifts and are based on our photometry. Q0738+313 lists luminosities in K' .

^cMorphology codes: Dd – Disk dominated; D – Disk; B+D – Bulge plus Disk; B – bulge; P – unresolved; blank – unknown type

^dThe profile linear scale length assuming object is at absorber redshift

^eObservations were non-photometric.

^fValues correspond to $z_{\text{abs}} = 0.0912$ and $z_{\text{abs}} = 0.2212$ respectively.

^gValues corresponds to $z_{\text{abs}} = 1.282$